10

Complementary Approaches and Time Series

10.1 Complementary Approaches

In Chapters 5, 6, and 7 we discussed repeat-pass radar interferometry for measuring the range component of surface deformation, which corresponds to the line of sight (LOS) vector between a point on the ground and the satellite. In Chapter 11 we discuss how deformation measurements can be combined from ascending and descending orbits to obtain two LOS components of deformation in cases where the deformation event occurs as a step function in time (e.g., earthquake). However, two components do not resolve the full vector motion, and the deformation may not occur as a step function in time. Moreover, the magnitude of the deformation gradient may exceed the capabilities of the InSAR system (i.e., greater than $\sim\pi$ radian per pixel) and/or the extreme deformation event may result in InSAR decorrelation. In these cases, methods have been developed to provide this additional information. We discuss these complementary approaches in this chapter.

We first review SAR image cross-correlation methods to recover large displacements in the range and azimuth directions. At best, these approaches can recover deformation to a precision of 1/10 of a pixel, so they are mainly used for estimating large deformations (0.5–10 m). Of course, the range measurement is in the same LOS direction as the interferogram, so this measurement is most useful to augment the interferogram in regions of large displacement gradient and/or decorrelated areas. The azimuth measurement is parallel to the ground track and perpendicular to the range measurement so provides new vector information (Fialko et al., 2001; Wright et al., 2004), but the precision is limited to about 1/10 of an azimuth pixel. The same azimuth component of deformation can be derived at a somewhat higher accuracy using multiple aperture interferometry (MAI) as discussed in Section 10.3.

The remainder of the chapter discusses methods for combining a set of interferograms derived from many SAR images to recover deformation time series with

either uniform velocity in time (stacking, Section 10.4) or with a nonuniform time history (i.e., small baseline subset methods (SBAS), Section 10.5). Section 10.6 discusses methods for reconstructing displacement time series in regions where there is significant decorrelation. This is accomplished by first identifying pixels that remain coherent over long time periods; these pixels have stable amplitude and phase, so they are called persistent scatterers (PS).

10.2 Range and Azimuth Pixel Offsets

Surface deformation between a reference and repeat image produces localized pixel displacement relative to the pixels within the larger image. This can be used to measure deformation and the approach is called *pixel offset tracking* (POT). This approach was originally developed to measure deformation in repeated optical images (e.g., Van Puymbroeck et al., 2000) and can also be used for measuring deformation from repeated SAR images. Indeed, the optical and SAR approaches are often combined to improve overall accuracy and coverage of surface deformation (He et al., 2023).

As discussed in Section 3.7.3, the reference and repeat images must first be aligned to subpixel accuracy to achieve high interferometric coherence. This can be accomplished using either geometric alignment based on precise orbits or 2-D complex cross-correlation of small patches typically 64 by 64 pixels. (Larger patches will provide a more robust offset estimate but will use more computer time.) Let $C_1\,(r,a)$ be a patch from the reference SLC image and $C_2\,(r,a)$ be a patch from the repeat image where r and a are the range and azimuth coordinates, respectively. The normalized 2-D cross-correlation function is

$$\gamma\,(\Delta \mathrm{r}, \Delta \mathrm{a}) = \frac{C_1 ** C_2^*}{\sqrt{C_1 C_1^*}\sqrt{C_2 C_2^*}}. \tag{10.1}$$

where the $**$ operation represents a 2-D convolution and $\sqrt{C_1 C_1^*}$ is the amplitude in the reference image (at zero shift). The location of the peak in the cross-correlation function provides an estimate of the displacement between the two images $(\Delta \mathrm{r}, \Delta \mathrm{a})$, while the strength of the correlation peak provides an estimate of the reliability of the offset estimate. (As a practical note, the mean is removed from each patch and the edges are zero-padded to minimize edge effects.)

Note that the convolution theorem can be used to replace the numerically slow 2-D convolution with the product of the Fourier transforms given by

$$\gamma\,(\Delta \mathrm{r}, \Delta \mathrm{a}) = \frac{\mathcal{F}_2^{-1}\left[\mathcal{F}_2\,(C_1)\,\mathcal{F}_2\left(C_2^*\right)\right]}{\sqrt{C_1 C_1^*}\sqrt{C_2 C_2^*}}. \tag{10.2}$$

The patches could be complex numbers taken from the SLCs of the reference and repeat images or SAR amplitude images. To avoid aliasing, the amplitude images should be oversampled by two times (Werner et al., 2005). These functions (Equations (10.1) and (10.2)) are available in the GMTSAR program *xcorr* and there are many options for setting the patch size, the oversampling of the amplitude data, and the oversampling factor for the cross-correlation output.

If there is a large amplitude deformation within the prealigned images, the local offset estimates are a measure of local surface deformation (Zitova and Flusser, 2003). This method is called pixel offset tracking and compared to the interferometric approach, POT is better suited for larger displacements and is more tolerant to decorrelations (Werner et al., 2005; Colesanti and Wasowski, 2006) (Figures 10.1 and 10.2). For example, in the case of a large earthquake, the InSAR phase is often decorrelated in the epicentral area of extreme ground shaking (Figure 10.1(a)). However, pixel offset tracking can provide deformation measurement even at the rupture trace (Figure 10.1(b/c)).

Theoretically, the interferometric approach can only detect deformation at a maximum deformation gradient of $\sim\pi$ radians per pixel, especially considering the noise in the data, but there is no upper limit for pixel offset tracking. For example, the very first applications using SAR images to track glacier streams were using interferometry (Goldstein et al., 1993; Massonnet and Rabaute, 1993; Joughin et al., 1996a; Rignot et al., 1997), but soon scientists determined that offset tracking performs well even on very fast-flowing ice streams (Strozzi et al., 2002), and can potentially detect seasonal velocity changes (Sundal et al., 2011).

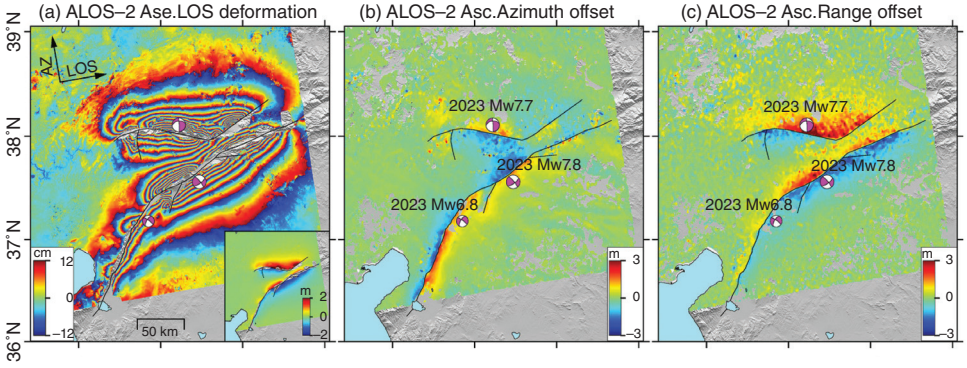

Figure 10.1 Deformation of the 2023 Turkey earthquake doublet derived by ALOS-2 ScanSAR data (He et al., 2023). (a) is the measured radar phase with the inset map being unwrapped LOS deformation. (b) is the azimuth offset with (c) being range offset.

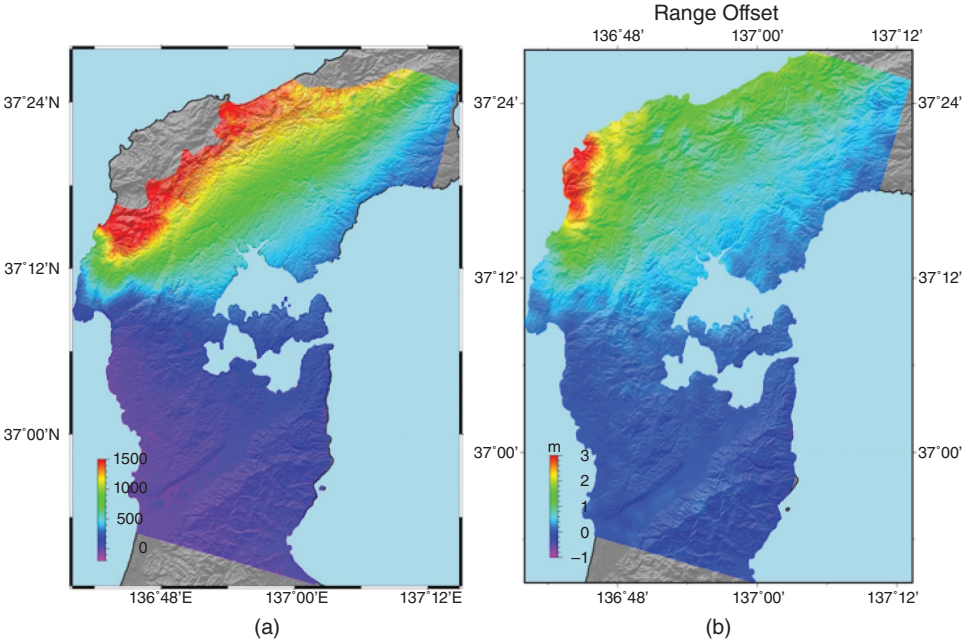

Figure 10.2 (a) unwrapped interferogram for the 2024 Noto Earthquake in Japan using ALOS-2 stripmap data, masked areas close to the shorelines are solutions with unwrapping errors due to strong shaking of the earth's surface. (b) Range offset estimate using POT can help acquire displacement estimates even at area with strong decorrelation. Adapted from Schmidt and Bürgmann (2003).

10.3 Multiple Aperture and Burst Overlap Interferometry

Azimuth offsets can be estimated using a completely different approach called *multiple aperture interferometry* (MAI) (Bechor and Zebker, 2006). Consider a localized surface displacement in the azimuth direction having a magnitude of x. Suppose the SAR is focused at a forward squint angle on the ground of θ_f and the localized deformation is imaged before and after the event. An interferogram constructed from the reference and repeat images will have a localized phase corresponding to the small component of deformation projected into the squinted LOS vector of $\phi_f = \frac{4\pi}{\lambda} x \sin\theta_f$ where λ is the radar wavelength (Bechor and Zebker, 2006). For a large magnitude of azimuth deformation (~1 m) and a nominal squint angle of a fraction of a degree, this phase change will be small, and the interferogram will be dominated by much larger phase distortions due to the troposphere and ionosphere. The MAI approach deliberately filters a single SAR image into a forward-looking image and a backward-looking image so two sub images are available. Then one constructs the forward and backward interferograms and computes their difference as

$$\phi_f - \phi_b = \frac{4\pi}{\lambda} x \left(\sin\theta_f - \sin\theta_b\right) \tag{10.3}$$

The phase changes due to the atmospheric and ionospheric effects largely cancel in the difference interferogram, while the phase change due to the along-track motion is doubled. Since the change in squint angle is related to the Doppler spectrum, a zero-Doppler SAR image, having an azimuth bandwidth of the PRF, can be decomposed into forward and backward-looking images with a band-pass filter in the azimuth direction (Scheiber and Moreira, 2000).

Thus, the computation for MAI interferograms involves three steps. The first step is to filter the full aperture SAR data into forward-looking and backward-looking subbands (along the track direction or column-wise). This is done on both reference and repeat SAR images. During this step, one should also compute the spectral separation between the forward-looking and backward-looking subbands (i.e., Δf). The second step is to compute interferograms between the forward-looking reference and forward-looking repeat and the backward-looking reference and backward-looking repeat subband datasets. Then one will be able to derive the azimuthal deformation with Equation 10.4

$$\Delta a = \frac{\mathrm{PRF}\left(\phi_f - \phi_b\right)}{2\pi\Delta f} \tag{10.4}$$

where PRF is the pulse repetition frequency. The azimuth pixel shift is converted to pixel shift in meters by multiplying by the ground-track pixel size $l_a = V_g/\mathrm{PRF}$ where V_g is the ground track velocity. Figure 10.3 shows examples of azimuthal deformation estimated using this MAI technique in comparison with pixel offset tracking; theoretically they should be equal, but there are practical issues associated with each approach.

Essentially, the MAI technique maps any azimuthal change into the double difference radar phase, and it does not differentiate whether it is caused by true ground deformation, along-track orbit error, or bias from the ionosphere. The bending of the radar beam caused by variation in the ionosphere can be assumed as a linear function related to the azimuthal gradient of the ionospheric phase as described in Liang and Fielding (2017)

$$\phi_{MAI-iono} = a\frac{\partial\phi_{iono}}{\partial a} + b \tag{10.5}$$

where a and b are coefficients of the polynomial fit to the gradient in the TEC of the ionosphere. Thus, the removal of this effect depends on the accurate estimates of

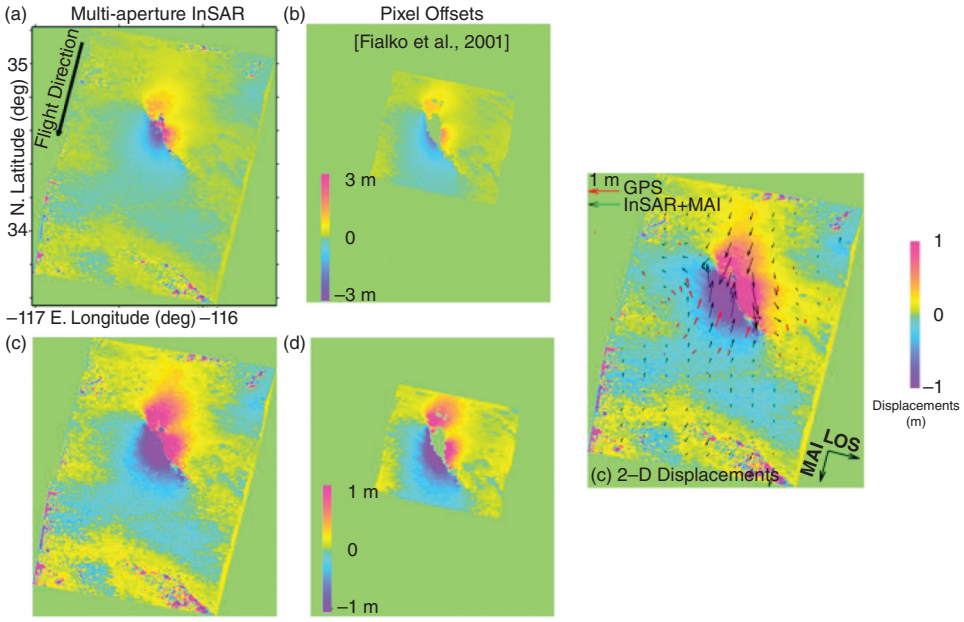

Figure 10.3 Multiple aperture interferograms (a and c) and their corresponding pixel offsets estimate (Bechor and Zebker, 2006). (b) The along track and InSAR LOS measurements with black arrows and GNSS vector measurements in red arrows. Do note the GNSS arrows are projected into radar LOS for comparison purposes.

the ionosphere (Figure 10.4). Since the quality (and coherence) of a subband interferogram is generally lower than the original full-bandwidth interferogram, and the ionospheric estimate also depends heavily on the coherence of the interferogram, thus such a method is usually considered only viable for good quality SAR data.

The underlying theory of the MAI technique takes advantage of the frequency separation between the forward-looking and backward-looking radar beams. Nonetheless, this separation can also be achieved with an intentionally steering the antenna as described in Section 8.5 on TOPSAR (Figure 8.7). Due to the designed sweeping antenna, the induced frequency separation is much larger than the PRF bandwidth of a strip-mode SAR. With such a design, this larger frequency separation makes double-difference phase more sensitive to any azimuthal motion or misregistration, but at a cost that this calculation can only be achieved at the 2-km-wide burst overlap area in the SAR image. This is referred to as *burst overlap interferometry* (BOI).

Thus, when one aims to measure azimuthal motion to form a 3-D displacement field with BOI, interpolation has to be made using the intermittent measurements. An example of such analysis is shown in Figure 10.5. Due to its high sensitivity

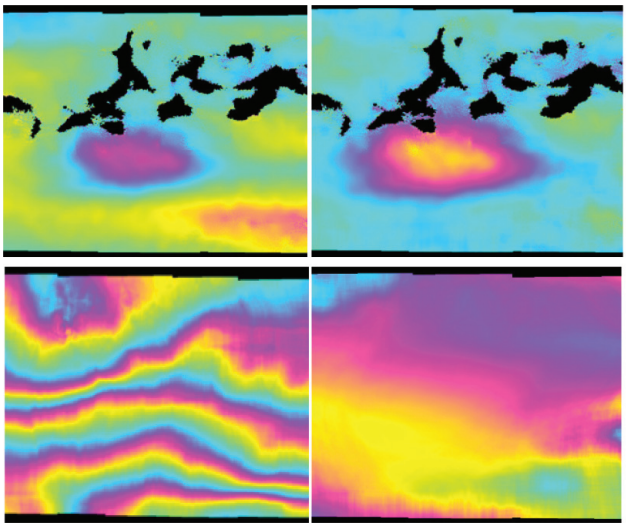

Figure 10.4 MAI interferogram estimated for the 2015 Nepal earthquake using ALOS-2 ScanSAR data (Liang and Fielding, 2017). Top left is the MAI interferogram without ionospheric phase correction using a two-burst cycle length ($2T_C$). Top right is the MAI interferogram with the ionospheric phase corrected. Bottom left is the ionospheric phase estimated using the range split-spectrum method used for correction. Bottom right is the estimated ionospheric effect in the MAI interferogram using Equation 10.5. Reprinted with permission from *IEEE Transactions on Geoscience and Remote Sensing*.

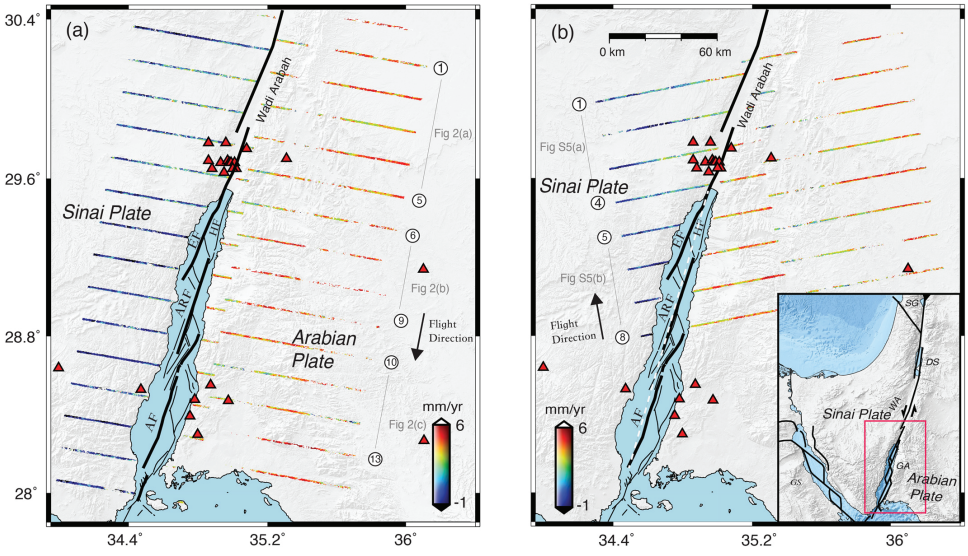

Figure 10.5 Along-track velocity derived from burst overlap interferometry (Li et al., 2021).

to azimuthal motion, such a technique is now also used to map subtle interseismic deformation as small as a few millimeters per year (Li et al., 2021) and mapping plate motion in a global framework (Lazeckỳ et al., 2023).

10.4 Stacking Approach

An interferogram measures surface deformation that occurred between the two SAR acquisition times along the radar LOS direction, and the stacking approach solves for the surface deformation rate by averaging interferograms with sufficient phase coherence that contain the common deformation signal of interest. More specially, the average LOS velocity v_{avg} of each ground pixel over a time period of interest T can be calculated as (Sandwell and Price, 1998):

$$v_{avg} = \frac{\sum_{i \in G} d_i}{\sum_{i \in G} t_i} \tag{10.6}$$

where G is a subset of coherent interferograms that were formed using two SAR scenes acquired within the time period T. The LOS measurement (in meters) and the temporal baseline of the i^{th} interferogram in G are written as d_i and t_i, respectively. To analyze how surfaces deform over time, we can solve for the average LOS velocities over multiple periods of interest using Equation 10.6. Over each period of interest T_j, we compute the cumulative LOS surface deformation over this period as the product of $v_{avg,j}$ and T_j.

Averaging interferograms that contain the common deformation signal of interest reduces the impact of random noise (e.g., tropospheric turbulence noise) by $\sim \sqrt{S}$, where S is the number of independent SAR acquisitions used in stacking. Alternatively, averaging interferograms that are formed using a particular SAR scene provides a way to characterize the InSAR noise term associated with that SAR acquisition. Under the assumption that spatially coherent tropospheric noise is the primary error source, the observed InSAR phase ϕ_{rn} at an interferogram pixel can be written as (Hanssen, 2001):

$$\phi_{rn} \approx \frac{4\pi}{\lambda}(d_{rn} + a_n - a_r) \tag{10.7}$$

where λ is the radar wavelength and d_{rn} is the LOS deformation $(d_n - d_r)$ between two SAR acquisition dates r and n. The tropospheric noise along the LOS direction on the two SAR acquisition dates is a_r and a_n, respectively.

We can generate up to $S-1$ interferograms using a common-reference SAR scene r (Tymofyeyeva and Fialko, 2015) from S SAR scenes over an area of interest. We define the common scene stacking (CSS) solution of size K as the average of a subset of K interferograms (Zebker et al., 2023):

$$\begin{aligned}\overline{\mathrm{S}}_{r,K} &= \frac{\lambda}{4\pi K}\sum_{n\in G, n\neq r}\phi_{rn} \\ &\approx \frac{1}{K}\sum_{n\in G, n\neq r} d_{rn} - a_r + \frac{1}{K}\sum_{n\in G, n\neq r} a_n\end{aligned} \tag{10.8}$$

where G is a set of SAR acquisitions that were used to form K ($K \leq S-1$) randomly selected interferograms with a common-reference SAR acquisition r.

The CSS solution $\overline{\mathrm{S}}_{r,K}$ contains three terms: the sum of LOS deformation signals of the K interferograms, the tropospheric noise a_r on the reference date r, and the average tropospheric noise of all other acquisition dates in G. Because tropospheric noise is typically not correlated beyond a few hours (Emardson et al., 2003), the term $\sum_{n\in G, n\neq r} a_n$ approaches zero when K is sufficiently large. In this scenario, $\overline{\mathrm{S}}_{r,K}$ only contains the sum of deformation signals and $-a_r$. In the case that no deformation signal is present in a dataset, the common-reference stacking solutions derived from randomly selected interferogram subsets converge to $-a_r$ as K increases.

While the deformation term d_{rn} is typically different in these K interferograms with a common-reference scene r because of different temporal baselines, the tropospheric noise term a_r remains the same. When the common-reference stacking solutions derived from randomly selected interferogram subsets do not converge, the differences between these subset stacking solutions can be used to determine the temporal characteristics of the deformation signal. For the linear deformation case, Tymofyeyeva and Fialko (2015) developed a method to separate deformation signals and noise. A common-reference stacking solution of a forward K subset as the average of K forward interferograms:

$$\overline{\mathrm{F}}_{r,K} = \frac{\lambda}{4\pi K}\sum_{n=r+1}^{r+K}\phi_{rn} \approx \frac{1}{K}\sum_{n=r+1}^{r+K} d_{rn} - a_r \tag{10.9}$$

where the reference date r is earlier in time than the nonreference date n for a forward interferogram. Similarly, a common-reference stacking solution of a backward K subset is defined as the average of K backward interferograms:

$$\overline{\mathrm{B}}_{r,K} = \frac{\lambda}{4\pi K}\sum_{n=r-K}^{r-1}\phi_{rn} \approx \frac{1}{K}\sum_{n=r-K}^{r-1} d_{rn} - a_r \tag{10.10}$$

where the reference date r is later in time than the nonreference date n for a backward interferogram.

By combining Equations 10.9 and 10.10, we eliminate a_r and estimate the average deformation rate, v_r, between SAR acquisitions $r-K$ and $r+K$ as:

$$
\begin{aligned}
v_r &\approx \frac{K}{T_{tot}}(\overline{\mathrm{F}}_{r,K} - \overline{\mathrm{B}}_{r,K}) \\
&\approx \frac{1}{T_{tot}}\left(\sum_{n=r+1}^{r+K} d_{rn} - \sum_{n=r-K}^{r-1} d_{rn}\right)
\end{aligned}
\tag{10.11}
$$

where T_{tot} is defined as the total time spanned by all interferograms as:

$$
T_{tot} = \sum_{n=r+1}^{r+K} \Delta t_{rn} + \sum_{n=r-K}^{r-1} |\Delta t_{rn}| \tag{10.12}
$$

For a backward interferogram ($n < r$), Δt_{rn} is negative. Similarly, we eliminate the deformation term and estimate the tropospheric noise term as:

$$
a_r \approx -\frac{1}{2}(\overline{\mathrm{F}}_{r,K} + \overline{\mathrm{B}}_{r,K}) \tag{10.13}
$$

The sum of deformation signals in the forward and backward K interferogram subsets equals zero when (1)$\sum_{n=r+1}^{r+K} \Delta t_{rn}$ equals $\sum_{n=r-K}^{r-1} |\Delta t_{rn}|$ and (2) the deformation signal is linear in time. The presence of nonlinear deformation signals can lead to differences in solutions derived from Equation 10.13 for different K values. These differences can be used as a measure of the uncertainty in the tropospheric noise estimates (Zebker et al., 2023).

10.5 Small Baseline Subset Method

Berardino et al. (2002) and Schmidt and Bürgmann (2003) developed the SBAS approach for reconstructing surface deformation time series from a stack of interferograms. Here we review how the SBAS algorithm works. Suppose we want to solve for the unknown LOS phase history $\phi(t)$ at a ground pixel as shown in Figure 10.6. The i^{th} interferogram formed from two SAR scenes acquired at t_m and t_n measures the unwrapped phase $\Delta\phi_i$ at this pixel. Assuming the topography-related phase has been removed, $\Delta\phi_i$ can be related to the LOS deformation d_i that occurred between two SAR acquisition times t_m and t_n as:

$$
\Delta\phi_i = \frac{4\pi}{\lambda}(d_i + n_i) \approx \frac{4\pi}{\lambda}\sum_{l=m}^{n-1} m_l \tag{10.14}
$$

where λ is the radar wavelength, n_i is the noise term of the i^{th} interferogram, and m_l is the unknown LOS deformation at the l^{the} epoch between SAR acquisition times t_l and t_{l+1}.

An interferogram can measure $\Delta\phi_i$ in Equation 10.14 with negligible topographic or spatial decorrelation error only if the spatial baseline (the distance

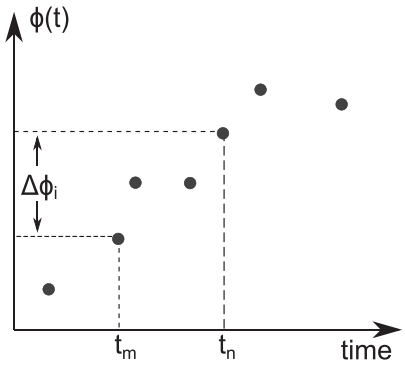

Figure 10.6 An LOS phase history we want to solve for at a given ground pixel location. The phase in a single interferogram formed from SAR data acquired at t_m and t_n measures $\Delta\phi_i$. Adapted from Tong and Schmidt (2016).

between the satellite locations at two SAR acquisition times) is small. The interferogram correlation becomes zero when the baseline component perpendicular to the LOS direction (perpendicular baseline) is larger than the critical baseline B_c, defined as:

$$B_c = \frac{\lambda \rho}{c\tau} \tan\theta \tag{10.15}$$

where ρ is the range between the radar satellite and the ground pixel, λ is the signal wavelength, θ is the radar incidence angle, c is the speed of light, and τ is the radar pulse length. In practice, an interferogram with a perpendicular baseline smaller than B_c may still suffer from severe decorrelation artifacts (e.g., due to vegetation growth). To limit phase decorrelation noise in the final time series, the SBAS method selects coherent interferograms as input data based on user-defined temporal and spatial baseline thresholds. These thresholds depend on the specific site characteristics and radar system parameters (e.g., radar wavelength), and it is recommended to include as many coherent InSAR phase measurements as possible in the SBAS inversion. This is because (1) interferograms with longer temporal baselines often contain larger secular deformation signals and (2) random phase noise tends to decrease as the number of coherent InSAR observations increases.

The formulation of the SBAS inversion is shown schematically in Figure 10.7. Given $S+1$ SAR images forming N interferograms with small baselines, we can define a matrix representation of the N-equation SBAS system as:

$$Gm = d \tag{10.16}$$

where $m = [\ m_1\ \ldots\ m_S\ ]^T$ is the vector of S unknown LOS deformation between each consecutive SAR acquisition, and $d = [\ d_1\ \ldots\ d_N\ ]^T$ is the vector of N known InSAR observations at the pixel of interest. The $N \times S$ design matrix G is also called

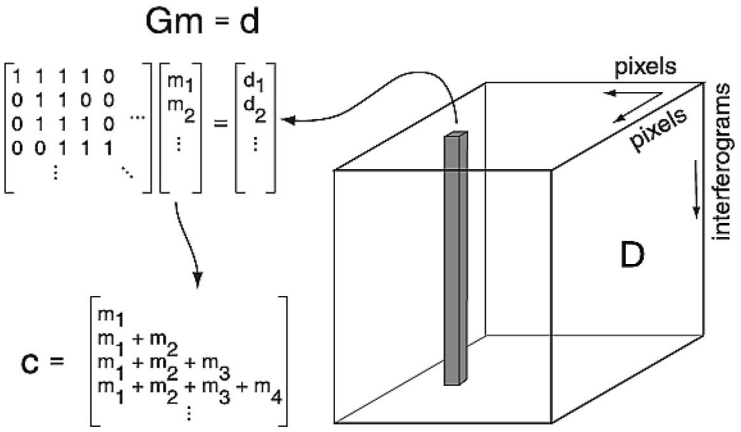

Figure 10.7 Schematic showing the relationship between InSAR phase data and model vectors in the SBAS inversion. From Schmidt and Bürgmann (2003).

the SBAS matrix. If the i^{th} interferogram measures the InSAR phase $\Delta\phi_i$ between SAR data acquisition times t_m and t_n as defined in Equation 10.14 at the pixel of interest, the i^{th} row of G has ones in the l^{th} entry for $l = m, \ldots, (n-1)$ and zeros in the remaining entries.

The vector m in Equation 10.16 can be approximately solved as:

$$m = G^{\dagger} d \tag{10.17}$$

where $G^{\dagger}$ is any generalized inverse of G. Here we choose $G^{\dagger}$ as the Moore–Penrose pseudoinverse, which can be efficiently computed using the singular value decomposition (SVD). A running sum of the incremental LOS deformation m_l yields the LOS deformation time series at the k^{th} epoch $C_k = \sum_{l=1}^{k} m_l$ at the pixel of interest.

Under the assumption that tropospheric noise can be approximated as random in time, we introduce a temporal smoothness constraint reduce tropospheric noise signatures in the LOS deformation estimates, and solve a regularized least squares problem as:

$$\begin{bmatrix} 1 & 1 & 0 & \cdots & \beta B_1 \\ 0 & 1 & 1 & \cdots & \beta B_2 \\ \vdots & \vdots & \vdots & \ddots & \vdots \\ \frac{\lambda}{\Delta t_1} & -\frac{\lambda}{\Delta t_1} & 0 & \cdots & 0 \\ 0 & \frac{\lambda}{\Delta t_2} & -\frac{\lambda}{\Delta t_2} & \cdots & 0 \\ \vdots & \vdots & \vdots & \ddots & \vdots \\ 0 & \cdots & \frac{\lambda}{\Delta t_{S-1}} & -\frac{\lambda}{\Delta t_{S-1}} & 0 \end{bmatrix} \begin{bmatrix} m_1 \\ m_2 \\ \vdots \\ m_S \\ \Delta h \end{bmatrix} = \begin{bmatrix} d_1 \\ d_2 \\ \vdots \\ d_N \\ 0 \\ \vdots \\ 0 \end{bmatrix} \tag{10.18}$$

Here λ is the temporal smoothing factor that penalizes unrealistically large temporal variations in m. To give each epoch an equal weight in the inversion, λ is scaled by the corresponding temporal interval Δt_l of the consecutive SAR observations. The choice of the smoothing factor can be optimized using independent data such as the GPS surface deformation time series. This SBAS formulation allows the estimation of the error Δh in the digital elevation model (DEM) at the pixel of interest from InSAR data (Berardino et al., 2002) because: (1) Δh can lead to an error in the i^{th} InSAR LOS deformation observation Δd_i that is linearly proportional to the InSAR perpendicular baseline B_i and (2) the constant scaling factor β can be calculated from the radar wavelength, the incidence angle of the radar wave, and the distance from the radar to the ground.

To reduce decorrelation noise, we may also solve for m using a weighted least squares scheme (Tong and Schmidt, 2016):

$$WGm = Wd \tag{10.19}$$

Here W is a diagonal weight matrix defined as:

$$W = \begin{bmatrix} \gamma_1 & 0 & 0 & 0 & \cdots & 0 \\ 0 & \gamma_2 & 0 & 0 & \cdots & 0 \\ \vdots & \vdots & \vdots & \vdots & \ddots & \vdots \\ 0 & 0 & \cdots & \gamma_N & \cdots & 0 \\ \vdots & \vdots & \vdots & \vdots & \ddots & \vdots \\ 0 & 0 & 0 & 0 & \cdots & 0 \end{bmatrix} \tag{10.20}$$

where γ_i is the spatial phase coherence of the *ith* interferograms. An example of interseismic velocity derived from coherence-based SBAS is shown in Figure 10.8.

10.6 Persistent Scatterer Algorithms

Both stacking and SBAS time series analysis methods require that InSAR phase observations are sufficiently coherent at the pixel of interest. Changes in surface scattering properties (e.g., due to vegetation growth) between consecutive radar acquisitions lead to InSAR phase decorrelation noise (Zebker and Villasenor, 1992). Because InSAR phase measurements at severely decorrelated radar pixels can be considered as random wrapped phase values between 0 and 2π, they cannot be used to reconstruct spatially coherent surface deformation patterns. *Persistent scatterer* (PS) techniques (e.g., Ferretti et al. (2000); Hooper et al. (2004); Ferretti et al. (2011)) have been developed to identify radar pixels with minimal changes in surface scattering properties (e.g., man-made structures, rocks, and barren lands).

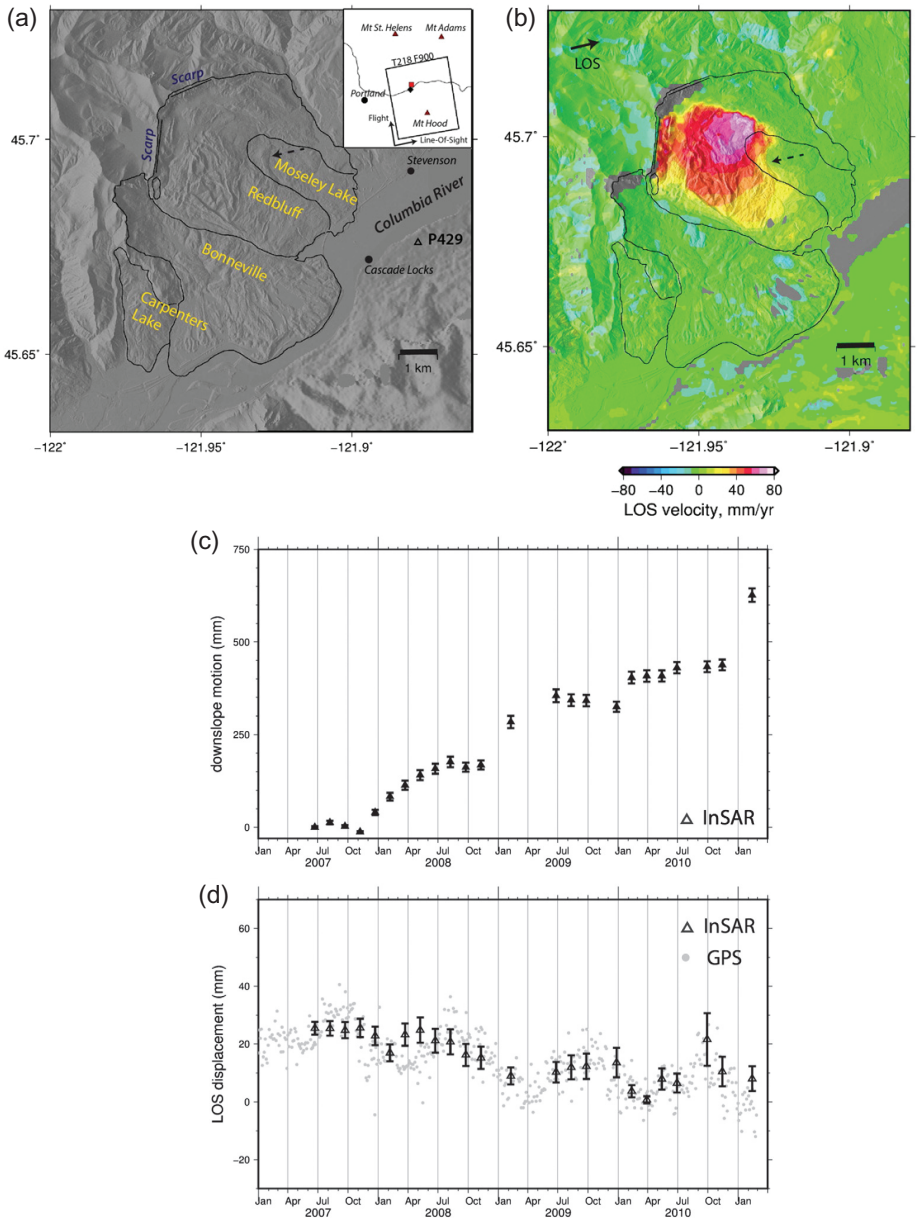

Figure 10.8 (a) Shaded relief map of the Cascade Landslide Complex and the Columbia River Gorge. The four main lobes of the landslide complex are outlined with black lines. A continuous GPS site is marked by the open triangle. The inset map shows the location of the Cascade Landslide Complex and the footprint of the ALOS-1 scene. (b) Average LOS velocity (a best-fit estimate to displacement time series) of the Cascade Landslide Complex. Warm colors indicate motion away from the satellite in the look direction (black solid arrow). (c) Cumulative downslope displacement in the deformation zone of the Red Bluff landslide from the InSAR time-series analysis. The location of the deformation time series is marked in (b). (d) Comparison of the InSAR time-series with a nearby GPS station P429. Gray dots show the daily position measured by the GPS and projected into the radar LOS direction for comparison. Negative LOS displacement corresponds to ground moving away from the satellite, that is, subsidence. The error bars of the LOS displacement are estimated from the standard deviations of the InSAR data within a 1 km window surrounding the sample location (Tong and Schmidt, 2016).

In areas with dense vegetation, only phase measurements at PS pixels have a high quality that is suitable for surface deformation time series analysis.

The first generation of PS algorithms (Ferretti et al., 2001; Lyons and Sandwell, 2003; Van Leijen, 2014) modeled radar echoes as the sum of a constant real signal and a complex circular Gaussian random noise. Based on this model, the returns from a radar pixel with a high signal-to-noise ratio (SNR) have relatively small amplitude variations. A pixel with high amplitude stability is identified as a PS pixel if its phase observations fit a given deformation model. One limitation of such approaches is that there are typically very few radar pixels with sufficient SNRs to be selected in natural terrain. To overcome this limitation, Hooper et al. (2004); Hooper and Zebker (2007); Shanker and Zebker (2007); Huang and Zebker (2019) selected PS pixels based on the statistics of InSAR phase measurements. Using a complex circular Gaussian model for both signal and noise terms, Shanker and Zebker (2007) estimated the signal-to-clutter ratio (SCR) of each radar pixel using phase measurements of interferograms that share a common reference SAR image. A PS pixel is expected to have a relatively high SCR and a narrow phase distribution. The capability of PS interferometry was further advanced by the SqueeSAR method (Ferretti et al., 2011; Goel and Adam, 2014; Lv et al., 2014). Ferretti et al. (2011) jointly analyzed nearby pixels with homogeneous amplitude distributions (referred to as statistically homogeneous pixels or SHP). The InSAR phase observations from each SHP group are averaged to improve SNR, and a covariance matrix model was employed to filter phase measurements and select PS pixels (Guarnieri and Tebaldini, 2008). The SqueeSAR-based approach is one of the very few existing methods that take into account the amplitude statistics of nearby distributed scatterers (DS). Alternatively, Costantini et al. (2008, 2014) modeled the phase difference between two adjacent radar pixels as a function of the deformation rate difference and elevation difference. For each neighboring pixel pair, an optimized deformation rate difference and elevation difference are solved to minimize the residual phase difference. The pixel pair is selected as PS if the residual phase difference is small. Because scattering signal models that take into account the phase correlation of nearby PS pixels have not been fully developed, existing PS selection algorithms are mainly based on the statistics of InSAR phase measurements at each individual radar pixel. In many cases, a deformation model (e.g., constant velocity) is employed in the selection process. However, surface deformation characteristics over the area of interest are often unknown. To overcome these limitations, a PS identification algorithm that analyzes the phase correlation of nearby radar pixels based on a similarity measure (the cosine similarity) was proposed (Wang and Chen, 2022). Here we give a review of the cosine similarity algorithm, which can be integrated with any existing PS selection algorithm to reduce the false positive and false negative PS selections at a very low computational cost.

Given K single look complex (SLC) radar images $S_1, \ldots, S_K$, $K-1$ wrapped interferograms that share a common reference SLC image can be formed. The phase values of these $K-1$ interferograms at a pixel m can be written as a phase vector $\boldsymbol{\varphi}_m = [\varphi_{m,1}, \varphi_{m,2}, \ldots, \varphi_{m,K-1}]$. We define the phase similarity between two radar pixels m and n as the cosine similarity between the phase vectors $\boldsymbol{\varphi}_m$ and $\boldsymbol{\varphi}_n$:

$$s_{mn} = \frac{1}{K-1} \sum_{k=1}^{K-1} \cos(\varphi_{m,k} - \varphi_{n,k}) \tag{10.21}$$

Here the phase similarity score s_{mn} ranges from -1 and 1. A similarity score of 1 means $\boldsymbol{\varphi}_m$ and $\boldsymbol{\varphi}_n$ are identical, 0 means $\boldsymbol{\varphi}_m$ and $\boldsymbol{\varphi}_n$ are not correlated, and -1 means $\varphi_{m,k}$ and $\varphi_{n,k}$ differ by π radians for all k's.

The cosine similarity algorithm is designed to retrieve accurate deformation signals over low-PS-density natural terrains. In this scenario, the deformation signal of interest is often caused by geophysical processes, including but not limited to coastal processes, aquifer pumping and recharge, volcanism, or fault activities. Because the Earth's crust can be modeled as a solid continuum, such surface displacements typically vary slowly in space (Segall, 2010). Because the deformation signal of interest and tropospheric noise are both spatially coherent, the phase vectors of two nearby PS pixels are expected to be similar (e.g. with phase similarity > 0.5). By contrast, the similarity score of a decorrelated pixel (a non-PS pixel) and a nearby pixel is ~ 0 when the total number of SAR acquisitions K is sufficiently large. This is because the phase of a decorrelated pixel can be considered as a random value between 0 and 2π (Zebker and Villasenor, 1992).

It is computationally expensive to calculate the phase similarity between all radar pixel pairs. To improve computational efficiency, a set of PS candidate pixels can be selected using an existing PS selection algorithm such as the maximum likelihood estimation (MLE) selection method (Shanker and Zebker, 2007). Following Shanker and Zebker (2007), the received echo from a radar pixel can be modeled as a coherent sum of returns from a dominant scatterer and clutter scatterers, and both components are considered as circular complex Gaussian random variables. The relative power of the dominant scatterer signal to the background clutter noise is defined as the signal-to-clutter ratio (SCR; γ). Based on this model, the probability density function (PDF) of the observed InSAR phase φ for a given SCR γ can be written as:

$$p(\varphi|\gamma) = \frac{1-\rho^2}{2\pi} \frac{1}{1-\rho^2\cos^2\varphi} \left(1 + \frac{\rho\cos\varphi \arccos(-\rho\cos\varphi)}{\sqrt{1-\rho^2\cos^2\varphi}}\right) \tag{10.22}$$

where ρ is defined as $\rho = 1/(1+\gamma^{-1})$. A PS pixel has a high SCR and a relatively narrow phase distribution, while a non-PS pixel has a low SCR and a relatively

wide phase distribution. The SCR value $\hat{\gamma}_{\mathrm{ML},m}$ at a given pixel m is estimated by comparing the observed InSAR phase vector $\boldsymbol{\varphi}_m$ to Equation 10.22 in a maximum likelihood sense:

$$\hat{\gamma}_{\mathrm{ML},m} = \arg\max_{\gamma} \prod_{k=1}^{K-1} p(\tilde{\varphi}_{m,k}|\gamma) \tag{10.23}$$

where $\tilde{\varphi}_{m,k}$ is the residual phase at pixel m in the k^{th} interferogram after removing the spatially correlated phase component through filtering. PS candidates are chosen as the pixels with $\hat{\gamma}_{\mathrm{ML},m} > 2$. This threshold value was suggested by previous SCR-based PS selection studies (Shanker and Zebker, 2007; Huang and Zebker, 2019; Adam et al., 2003; Chen et al., 2017) as a reasonable trade-off between the false positive and false negative rates. A higher $\hat{\gamma}_{\mathrm{ML},m}$ value leads to a lower false positive rate and a higher false negative rate.

During the preliminary PS candidate selection, the SCR value at each pixel is estimated independently. The spatial phase consistency between PS pixels is not taken into account, which may lead to inaccurate PS selections (Chen et al., 2017). To overcome this limitation, the false positive PS pixels in the current PS candidates pool are removed if their median cosine similarity score to their N nearest neighbor PS candidates is lower than a user-defined threshold. To further recover false negatives in the preliminary PS candidate pool, the phase similarity of every non-PS pixel m with its N nearest neighbor PS pixels is also calculated, and the pixel m is selected as a new PS if the maximum phase similarity is greater than a user-defined threshold. The search of false negative PS pixels is performed iteratively to expand the PS set, and the number of PS pixels increases monotonically through iterations. Because the number of detected PS pixels is upper-bounded by the total number of radar pixels, our algorithm is guaranteed to terminate when no more PS pixels can be identified through additional iterations. Because the phase vectors of two non-PS pixels are unlikely to be similar when the number of SAR acquisitions is sufficiently large (e.g., $K > 30$), the search for false negatives typically introduces very few false positive PS pixels. More discussion on the similarity threshold selection can be found in Wang and Chen (2022).

Once PS pixels are identified, an adaptive spatial interpolation can be employed between PS pixels (Chen et al., 2015) to reconstruct spatially coherent phase observations (including deformation signals and tropospheric noise). Given a wrapped interferogram, the phase value at pixel m is replaced by the weighted average phase value of its N nearest neighbor PS pixels as:

$$\varphi_m^{\mathrm{interp}} = \arg\left(\sum_{n\in \mathrm{NN}(m,N)} w_n e^{i\varphi_n}\right) \tag{10.24}$$

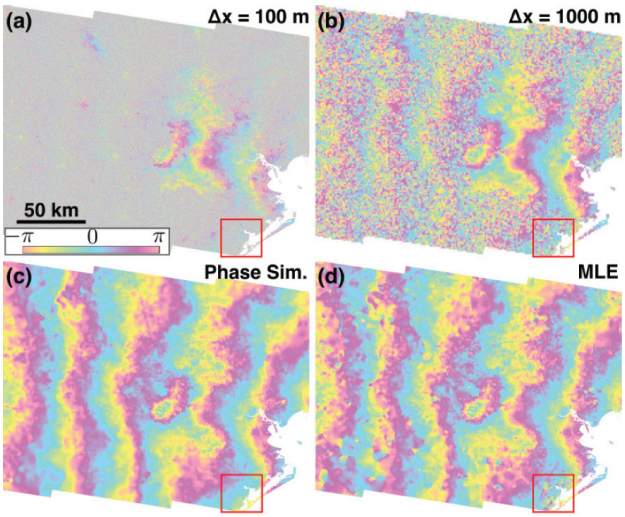

Figure 10.9 (a) 672-day Sentinel-1 interferogram (January 3, 2018–November 6, 2019) over the Greater Houston area (100-m pixel spacing). (b) Same interferogram with an additional 10 looks in both dimensions (1 000-m pixel spacing). (c) Interpolated interferogram using PS pixels identified by the phase similarity algorithm. (d) Interpolated interferogram using PS pixels identified by the MLE algorithm. From Wang and Chen (2022).

where $\arg(z)$ is the argument of the complex number z, $\mathrm{NN}(m,N)$ represents the N nearest neighbor PS pixels of pixel m, and φ_n is the wrapped phase value at pixel n. $w_n = e^{-r_n^2/2R}$, where r_n is the distance between the center pixel m and pixel n and $R = \max_n r_n$.

The PS interpolation method can not only fill the spatial gaps in high-quality InSAR phase measurementsi (Figure 10.9) but also substantially improve the accuracy and computational efficiency of phase unwrapping (Chen and Zebker, 2001). Additionally, PS interpolation can be used to evaluate the accuracy of PS selection. While accurate PS selection usually results in spatially smooth phase reconstruction, interpolation from inaccurate PS sets can cause abrupt phase changes near false positive PS pixels. Such phase artifacts can be easily identified through visual inspection or quantified by the phase unwrapping error at a radar pixel m defined as:

$$\varphi_m^{\mathrm{err}} = \sum_n |\Delta\varphi_{mn}| f_\pi(|\Delta\varphi_{mn}|) \tag{10.25}$$

where $\Delta\varphi_{mn}$ is the unwrapped phase difference between pixel m and pixel n (or $\varphi_m^{\mathrm{unwrap}} - \varphi_n^{\mathrm{unwrap}}$), f_π being an indicator function such that $f_\pi(x) = 1$ if $x > \pi$ and $f_\pi(x) = 0$ otherwise. The summation is performed on the four adjacent pixels of the center pixel m. The total phase unwrapping error of an interferogram is calculated as the sum of the phase unwrapping errors over all radar pixels.

10.7 Problems

1. An ice stream has a typical velocity of 2 m per year and was imaged by a C-band radar with a 12-day cadence. Why would the pixel offset tracking method provide better results than standard interferometry?
2. Derive Equation (10.4). Consider the relation between the squint angle and the corresponding Doppler caused by the moving platform.
3. What are the limitations of CSS? Consider a few scenarios in which such a technique fails to produce a valid estimate of atmospheric phase screens. One example is very strong atmospheric noise on two consecutive observation dates.
4. What complementary approach is best for measuring deformation in an area that is highly decorrelatead?
5. Create a synthetic deformation time series with a linear deformation signal of 1 cm/year. The first synthetic SAR scenes are acquired on day 0 and then every 12 days for a year. At each SAR acquisition, add a random Gaussian noise with a zero mean and standard deviation of 1 cm. Generate all possible InSAR pairs as your synthetic InSAR data at a pixel location. Using stacking and SBAS algorithms to solve for the deformation rate. Comment on the statistics of the estimation error based on 1 000 synthetic InSAR data vectors with different random noise samples. Now repeat the experiment with different set ups (e.g., 6-day revisit cycle or different noise levels) and comment on the results. If interferograms with a temporal baseline longer than 24 days are completely decorrelated, what is the impact on the results?